

Turbulence in counter-streaming paraxial superfluids of light

Myrann Abobaker
Master 2 internship at LKB, 2021
Supervised by Quentin Glorieux

July 8, 2021



Abstract

Quantum turbulence is a complex phenomenon observed in quantum fluids and difficult to study experimentally because of the high instability of these systems. This problem does not exist in quantum fluids of light which also benefits from a large toolbox for quantum detection. Many theoretical works like [1], [2] have been carried out on turbulence in quantum fluids of light but none about experimental results in hot atomic vapours.

My project focuses on this experimental realization and study complex hydrodynamic phenomena using the quantum fluids of light platform.

Specifically, I focus on the evolution of the interference generated by two counter-streaming laser beams in a hot atomic vapor. Under specific conditions the photons will behave like a fluid of light [3] and will follow the same dynamics as an atomic Bose-Einstein condensates.

The idea is that we can observe the same phenomena as in classical hydrodynamics thanks to this platform, i.e. cascading generations of vortex pairs [4] causing instabilities in the system.

This work provides a natural route towards the experimental investigation of quantum turbulence, instabilities, and out-of-equilibrium dynamics in superfluids of light.



Contents

1	Introduction	3
2	Photon fluid in the 2D+1 propagating geometry	4
2.1	Non-linear Schrödinger equation in optics	4
2.1.1	Propagation equation in a non-linear medium	4
2.1.2	Approximations	4
2.1.3	Comparison to the Gross-Pitaevskii equation	5
2.2	Hydrodynamic analogy	5
3	Atomic medium characterization	6
3.1	Tools	6
3.1.1	Rubidium cells	6
3.1.2	Laser	7
3.2	Temperature measurement	7
3.2.1	Transmission measurement	7
3.3	Frequency measurement	8
3.3.1	Saturated absorption Spectroscopy	8
3.4	Non-linear refractive index measurement	9
3.4.1	Interferometric method	9
4	Turbulence in 2 counter-streaming fluids of light	12
4.1	Dispersion relation	12
4.2	Experimental setup	13
4.2.1	SLM and fluids velocity control	14
4.2.2	Imaging of interferences evolution in the non-linear medium	14
4.3	Density distribution in the momentum space	15
5	Turbulent cascade and vortices	18
5.1	Optical vortices	18
5.2	Phase map and "forks"	19
5.3	From instabilities to turbulence	20
6	Conclusion	21

1 Introduction

Hydrodynamic phenomena are today difficult to model and their behaviour and evolution are open questions [5]. This is the case of turbulence, the study of which began in the 15th century with the works of Leonardo da Vinci. Since then, a lot of work has been done on this subject and models have been developed to explain it, such as the turbulent cascade governed by Kolmogorov's laws [4].

For the past few decades, research on quantum fluids like atomic Bose-Einstein condensates [6], which are composed of bosons all in a macroscopic quantum state, has been greatly developed. They have shown their usefulness in simulating hydrodynamic phenomena [7] but the problem is that it is difficult to make measurements on it without breaking the quantum state of the system.

A new community has recently emerged working on quantum fluids of light, optical systems where light behaves like a fluid according to hydrodynamic laws [8]. Fluids of light are a good platform because of their high tunability and repeatability compared to the Bose-Einstein condensates which requires a very large installation and is very unstable. Moreover, there are already many quantum optical detection tools with high efficiency which is not the case for atoms.

In specific media and conditions, light propagating in the paraxial approximations can be described as a fluid of light. In this case, the photons interact with each other and behave like massive bosons. The dynamic of the system is described by the non-linear Schrödinger equation which is analogous to the Gross-Pitaevskii equation used to describe quantum fluids such as the Bose-Einstein condensate [8]. Quantum fluids of light are therefore good candidates for quantum simulation because hydrodynamic phenomena such as blast waves [9], solitons [10] and turbulence [1] are possible in these systems.

In this work, I focus on the experimental realisation of the turbulence produced by two counter-streaming fluids of light. In addition, we study the evolution of interferences, especially instabilities and turbulence during the propagation of the fluids. The results are also compared with the theoretical predictions [1] by studying turbulence in the momentum distribution. In parallel, we observed vortices generated within them and their characterisation by reconstructing the phase of the electric field.

Acknowledgment : This internship was done in Quentin Glorieux's team at the Laboratoire Kastler Brossel (LKB) which contains 3 professors, 2 post-docs, 6 phd-student and 7 master students. Within this team I greatly appreciated our cohesion and simplicity of communication. Continuing my thesis in another team, I will miss them a lot but of course we will continue to work together. Thank you to Guillaume and Tangui for the discussion's, their Python code and for reviewing this report (even if they are maniacal, mostly you Guillaume!). All this work have been achieved with you Wei and I appreciated our team-work and mutual teaching. Good luck for the future. Don't worry we will continue to work together! Special thanks to Murad for his teaching, jokes and his marcel. And I don't forget you Tom, it was really productive to work with you, even when we were talking about stranges social behavior. And I don't forget to thank the polariton team, Ferdinand, Maxime, Kevin and Malo to be polariton's people... Additional thanks to Morgan for his theoretical help ;) And to finish, I really thank my supervisor, Quentin, for creating this healthy working environment, for the trust, respect and oportunity you gave me. I owe you a lot. I hope you will manage to escape from Paris one day :)

2 Photon fluid in the 2D+1 propagating geometry

In classical optics, photons do not interact with each other. However, in the non-linear case, photons can acquire an effective mass and begin to "see" each other. In this case, the evolution followed by the light is the same as that of quantum fluids such as an atomic Bose-Einstein condensates.

Thanks to these systems, it is possible to study many classical hydrodynamic phenomena only with photons and a non-linear medium.

2.1 Non-linear Schrödinger equation in optics

2.1.1 Propagation equation in a non-linear medium

In a non-linear Kerr-type medium the evolution equation of the electric field \mathbf{E} is given by:

$$\nabla^2 \mathbf{E} - \frac{1}{c^2} \frac{\partial^2 \mathbf{E}}{\partial t^2} = \frac{1}{\epsilon_0 c^2} \frac{\partial^2 \mathbf{P}}{\partial t^2}, \quad (1)$$

where c is the speed of light, ϵ_0 is the dielectric permittivity in vacuum and \mathbf{P} is the polarisation of the medium. In the case of a non-linear medium, the polarisation \mathbf{P} is written:

$$\mathbf{P}(\mathbf{r}, t) = \underbrace{\epsilon_0 \chi^{(1)} \mathbf{E}(\mathbf{r}, t)}_{\mathbf{P}_L(\mathbf{r}, t)} + \underbrace{\epsilon_0 \chi^{(2)} \mathbf{E}^2(\mathbf{r}, t) + \epsilon_0 \chi^{(3)} \mathbf{E}^3(\mathbf{r}, t) + \dots}_{\mathbf{P}_{NL}(\mathbf{r}, t)} \quad (2)$$

Susceptibilities $\chi^{(n)}$ are tensors of ranks $n + 1$ ($n \in \mathbb{N}$). The system is an isotropic, homogeneous, centro-symmetric atomic gas, thus all the even-order $\chi^{(2n)}$ vanish [11]. In addition, the higher order are neglected and we stop at $n = 3$.

For a monochromatic laser field $E(\mathbf{r}, t) = \frac{1}{2} (E_0(\mathbf{r})e^{i\omega t} + cc.)$ we can rewrite (1):

$$\nabla^2 E_0(\mathbf{r}) + k_0^2 \epsilon_r(\omega) E_0(\mathbf{r}) = -\frac{1}{2} \frac{\omega^2}{c^2} \chi^{(3)}(\omega) |E_0(\mathbf{r})|^2 E_0(\mathbf{r}), \quad (3)$$

with $\epsilon_r(\omega) = 1 + \chi^{(1)}(\omega)$ is the permittivity of the medium and k_0 is the laser wave-vector in vacuum. We define the linear index $n_0(\omega) = \sqrt{\text{Re}(\epsilon_r(\omega))}$ and the absorption coefficient $\alpha(\omega) = k_0 \frac{\text{Im}(\epsilon_r(\omega))}{n_0}$.

2.1.2 Approximations

Field propagation is limited for small angles near the optical axis (z -axis in our case) along which the beam propagates. In this case, the amplitude of the field varies slowly in the transverse plane (perpendicular to z) and the so-called paraxial approximation can be achieved. The field envelope is:

$$E_0(\mathbf{r}_\perp, z) = E_0(\mathbf{r}_\perp, z) e^{ik(\omega)z}, \quad (4)$$

where the amplitude is a slowly-varying function. \mathbf{r}_\perp is the spatial coordinate in the transverse plane. In this approximation, without an external potential and losses, the propagation equation of the field in a non-linear medium Kerr-type is:

$$i \frac{\partial E(\mathbf{r}_\perp, z)}{\partial z} = \left(-\frac{1}{2k_0} \nabla_\perp^2 + g |E(\mathbf{r}_\perp, z)|^2 \right) E(\mathbf{r}_\perp, z), \quad (5)$$

with $g = -k_0 n_2$ is the interaction term with $n_2 = \chi^{(3)}/(2cn_0^2\epsilon_0)$ the non-linear index. We define $\Delta n = n_2 |E|^2$ as the non-linear refractive index of the medium. It acts as an attractive or repulsive potential, depending on its sign. In the experiments we work in the repulsive regime for the stability. We avoid going into the attractive regime because the beam will self-focus very quickly and we will recover a beam cut into filaments [12]. (5) equation is also called the Non-linear Schrodinger Equation (NLSE).

2.1.3 Comparison to the Gross-Pitaevskii equation

We can establish a rigorous isomorphism to the Gross-Pitaevskii equation (GPE). For massive bosons in a trapping potential \mathcal{V} , the evolution time of a wave function Ψ is given by:

$$i\hbar \frac{\partial \Psi(\mathbf{r}, t)}{\partial t} = \left(-\frac{\hbar^2}{2m} \nabla^2 + \mathcal{V}(\mathbf{r}) + g|\Psi(\mathbf{r}, t)|^2 \right) \Psi(\mathbf{r}, t), \quad (6)$$

m is the bosonic mass and g the interaction parameter between bosons.

Space-time mapping: The main difference between equations (5) and (6) is that the GPE describes the evolution of the system along the real physical time, whereas the NLSE describes the space propagation. The idea, here, is that the z -direction plays the role of an effective time τ in the NLSE so that each transverse plane along the optical z -axis can be considered as a snapshot of the non-linear "time evolution" of the laser beam inside the medium. For each transverse plane, we define $\tau = zn_0/c$.

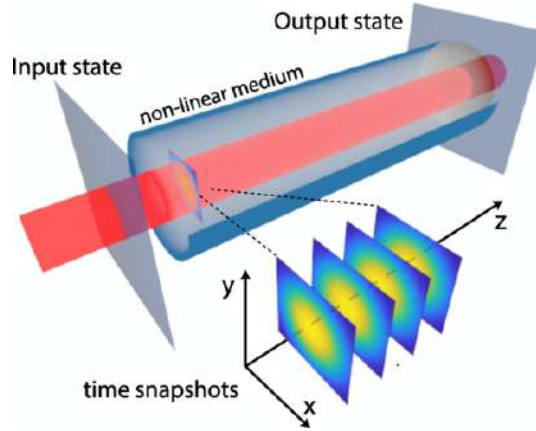


Figure 1: Propagation of a laser field along a non-linear medium like it is presented in [13]. For each transverse plane we take a time snapshot.

Finally, we can conclude from this that the NLSE describes the same physical situation as 2D Bose-Einstein condensates.

2.2 Hydrodynamic analogy

The NLSE can be mapped onto an hydrodynamic formulation by prescribing $E = \sqrt{\rho}e^{i\phi}$ with the fluid density $\rho = |E|^2$ (light intensity) and $\mathbf{v} = (c\nabla_{\perp}\phi)/k_0 = (ck_{\perp})/k_0$ the velocity field. By using this transformation, also called the Madelung's transformation [14], in the NLSE we can show that these quantities satisfy the hydrodynamic equations:

$$\begin{cases} \frac{\partial \rho}{\partial z} + \nabla_{\perp} \cdot (\rho \mathbf{v}) = 0, \\ \frac{\partial \mathbf{v}}{\partial z} + (\mathbf{v} \cdot \nabla_{\perp}) \mathbf{v} = -\frac{g}{k_0} \nabla_{\perp} \rho + \frac{1}{2} \nabla_{\perp} \left(\frac{1}{\sqrt{\rho}} \nabla_{\perp}^2 \sqrt{\rho} \right). \end{cases} \quad (7)$$

The first equation refers to the continuity equation. The second one is Euler equation. The last term in the second equation refers to the quantum pressure which is neglected in our experiments. With these equations we can now understand why the field, in a non-linear Kerr-type medium, can be called a quantum fluid of light.

3 Atomic medium characterization

We need a non-linear medium and a laser beam to have a fluid of light. Here I will focus on the medium and its characterization.

3.1 Tools

3.1.1 Rubidium cells

For all experiments, we used a Rubidium (Rb) atomic vapor. The main reason for using an alkali specie rather than other atoms is that it has an atomic transition in the near infrared, close to the wavelengths of the lasers, where the 2-level model is well suited.

The atomic structure of the Rb is also well known and it is developed in Q. Fontaine's thesis [3] from which this Fig.2 is extracted.

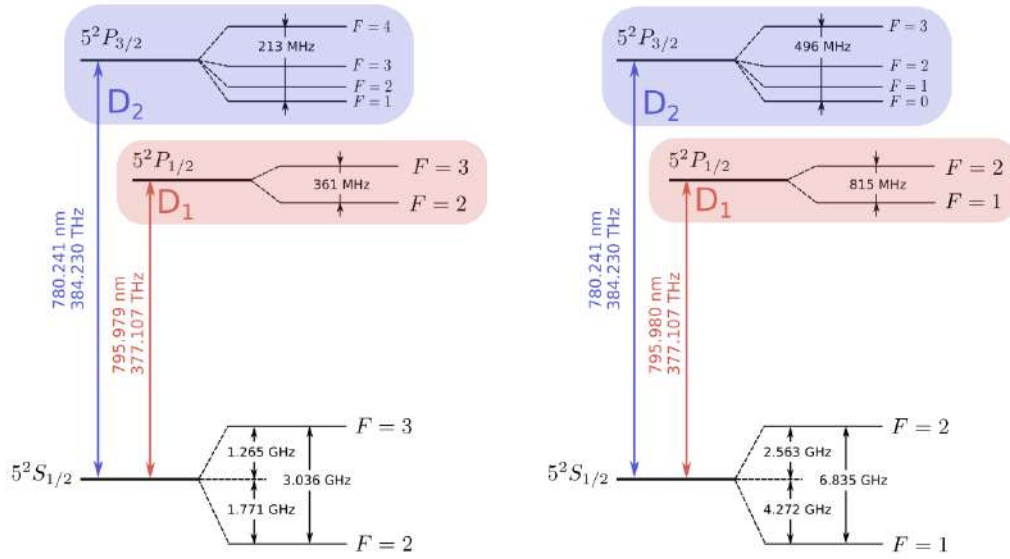


Figure 2: ^{85}Rb (left) and ^{87}Rb (right) D-line hyperfine structure.

The Rb vapor is contained in a cylindrical glass cell, closed on both sides by 1 mm thick anti-reflective coated windows at 780 and 795 nm suited for the laser wavelengths.

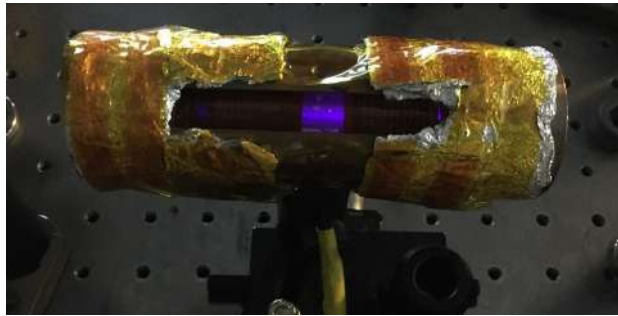


Figure 3: Picture of our cell containing the medium.

At room temperature Rb is solid so we wrap a resistance around the cell, as shown Fig.3, to heat the medium and have a homogenous atomic gases. Also by increasing the temperature, we increase the vapor pressure P_v and the atomic density N as shown Fig.17 from [3]. This is one of the knob we use to control the non-linearity of the medium because the susceptibilities $\chi^{(3)}$ depends on the atomic density [15]. For the experiment we work for temperatures between 100 and 150 °C. Below this level the non-linearity is too weak, above it is too strong and other undesirable phenomena come into play.

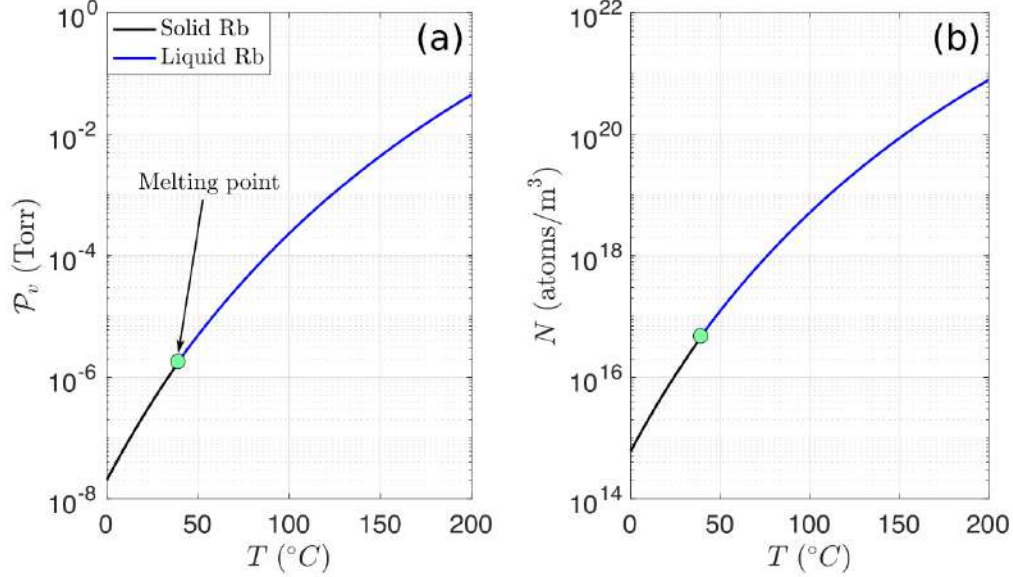


Figure 4: Vapor pressure (a) and atomic density (b) as function of temperature. The melting point of Rubidium is 39.31 °C. This is extracted from [3].

3.1.2 Laser

During the experiments we used a Muquans fiber laser bringing the laser beam directly through an optical fiber to our optical table.

Its wavelength is $\lambda_0 = 780.240$ nm (frequency is $\nu_0 = 384.229$ Thz).

We define the detuning $\Delta = \nu - \nu_0$. $\Delta = 0$ corresponds to the D2 transition of ^{85}Rb , shown Fig.2, starting from $F=3$ to $F'=2$.

We can control the detuning by using a function generator which allows us to have values of the latter over 10 GHz ($-5\text{ GHz} < \Delta < 5\text{ GHz}$). This function generator is linked to the laser and allow us to control the frequency by modulating the laser diode current (expliquer). Another possibility is to change directly the temperature of the diode. For other lasers like cavity lasers we can change the length of the cavity.

At the output of the optical fiber power is 1 W.

3.2 Temperature measurement

3.2.1 Transmission measurement

With a resistance we heat the medium but we don't know what is the precise value of the temperature of the gaz inside the cell. To measure its we record the transmission of the laser beam after it passage in the Rb cell while applying a frequency scan of 10 GHz. By changing the frequency, the beam is more or less absorbed depending on whether it is at a resonant frequency or not.

The data are shown Fig.5 and compared with the theory given by the fitted curve, based on the model from [16], which gives the temperature value. For the rubidium cell used here, the temperature value was 105.6 °C.

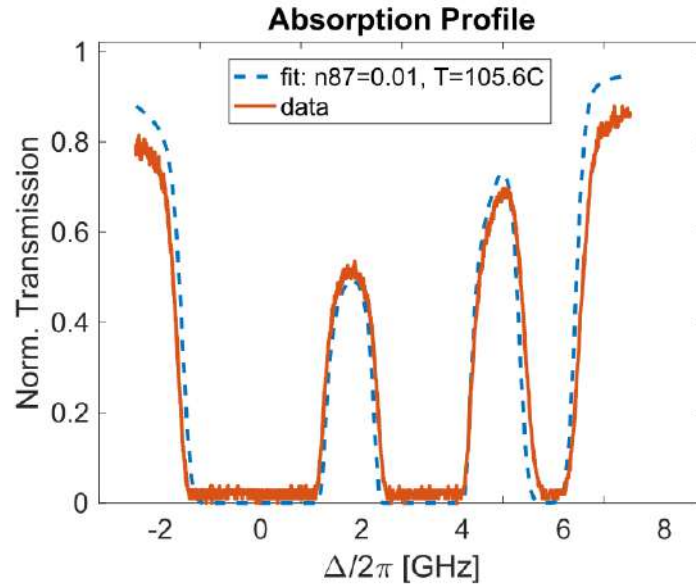


Figure 5: Temperature measurement with the mixed Rb cell 99% ^{85}Rb , 1% ^{87}Rb . The dashed curve is the fit. The red curve is from the experimental data. For these data $P = 1 \text{ mW}$.

3.3 Frequency measurement

3.3.1 Saturated absorption Spectroscopy

In the experiment, we work in the repulsive interaction regime which means that the interaction term has to be negative. So we detune the laser to negative value $\Delta < 0$.

We need to know the exact value of the detuning. To measure it we use a saturated absorption setup in addition to the experimental setup explained in section 4.2. Here, the difference with the temperature measurement is that we measure transmission on a photodiode the beam after his second passage in the Rb cell as shown Fig.6. This method allow us to minimise the Doppler effect because we only excite

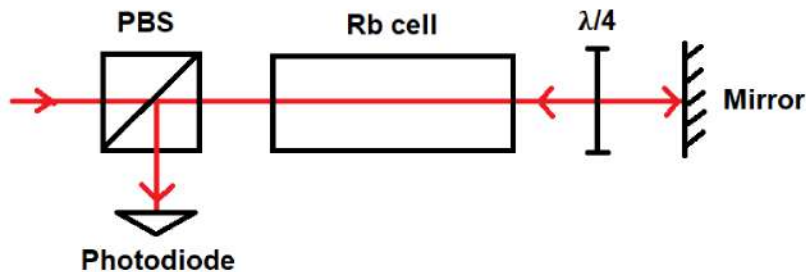


Figure 6: Saturated absorption setup.

atoms in the zero velocity class. This also allows us to distinguish resonances due to dipole-dipole

interactions [17].

By looking at the spectrum (Fig.7) and by knowing the frequency ramp and taking 2 points on the spectrum we can know the value of the laser frequency.

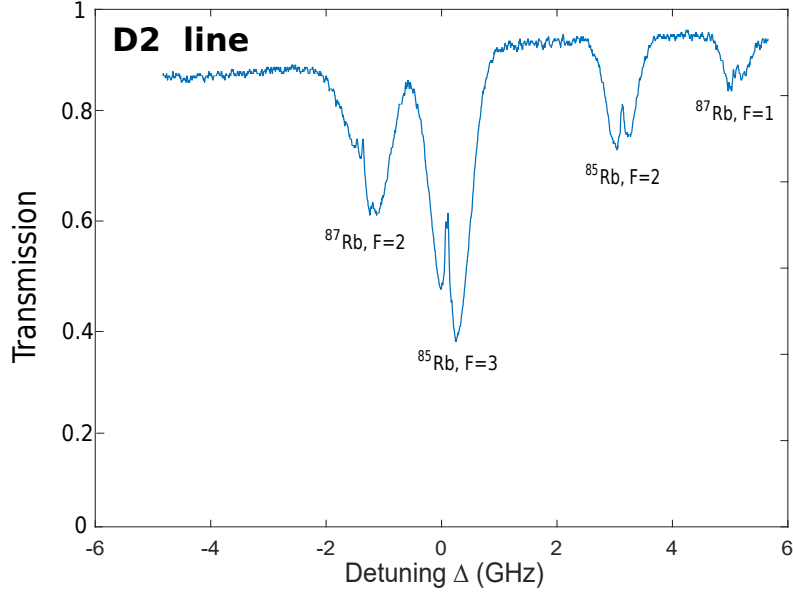


Figure 7: Saturated Absorption Spectrum of the Rubidium (87 and 85) D2 line. For these data $T = 105^{\circ}C$ and $P = 10$ mW.

3.4 Non-linear refractive index measurement

An important parameter that we need to calibrate the system is the non-linear refractive index of the medium Δn that we define earlier in section 2.1.2.

There are several methods to measure it like the far field method well explained in Q. Fontaine thesis and baser on [18]. Here I will present another method which is easy to apply and quite well developed now as it is widely used by the team members.

3.4.1 Interferometric method

The beam (close to the resonance $\Delta = -2$ GHz, called pump) passing through (shéma) the non-linear medium is made to interfere with a reference beam having a tilted angle in relation to the pump. Then, with a camera, which is imaging the output of the Rb cell, we observe the fringes like on Fig.8.

As we can see, by increasing the power we observe two phenomena: (i) an enlargement of the beam size (defocusing) because the beam diffracts faster [19] as usual. (ii) a curvature of the interference fringes which becomes more and more pronounced with the power and these are phase related. These 2 phenomena are due to the non-linear phase acquired by the beam during the propagation in the medium. This is well explained in [9].

Then we numerically analyse the data. From the curvature of fringes, we measure the accumulated non-linear phase $\Delta\phi$, according to the model in [20]:

$$\Delta\phi(\mathbf{r}, L) = k_0 L \frac{n_2 I(\mathbf{r})}{1 + \frac{I(\mathbf{r})}{I_s}} + \phi_0, \quad (8)$$

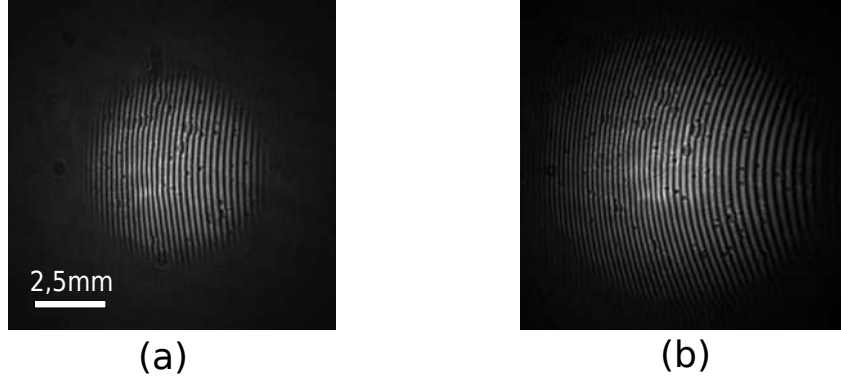


Figure 8: Interference fringes: (a) $P=30$ mW, (b) $P=600$ mW. For these data $\Delta = -2$ GHz and transmission is 5%, $T = 105^\circ C$.

where L is the cell length and I_s is the saturation intensity for which the value of the non-linear phase reaches a threshold [21]. $\Delta\phi$ is plotted in orange on Fig.9. The rest of the curve is a noise phase calculated and is not taken into account. The curve is plotted as a function of the radial coordinate of the beam. Here the waist of the pump beam is 0.4 mm.

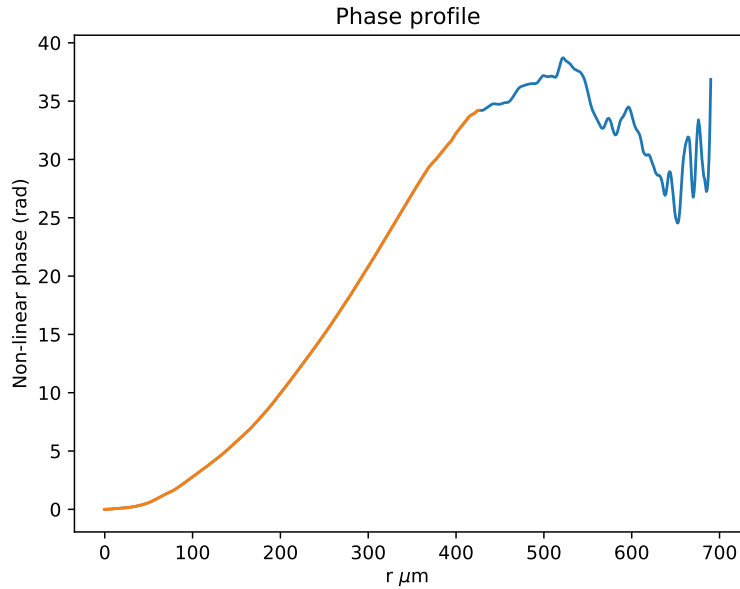


Figure 9: Phase profile as a function of the radial coordinate of the beam, $P=600$ mW. For these data $\Delta = -2$ GHz and transmission is 5%, $T = 105^\circ C$.

The origin corresponds to $\phi_0 = 0$. Then, we calculate the non-linear refractive index given by:

$$\Delta n = \frac{\Delta\phi}{k_0 L}. \quad (9)$$

The cell length is $L = 6.8$ cm. To characterize the non-linearity we plot Δn for 13 values on intensity. Finally we obtain Fig.10.

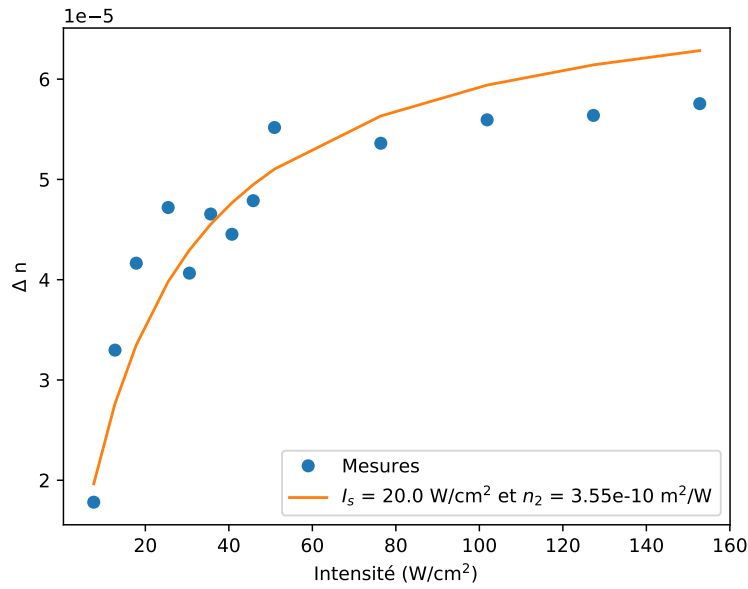


Figure 10: Δn as a function of the intensity. The fitted curve comes from analytical calculation. For these data $\Delta = -2$ GHz and transmission is 5%, $T = 105^\circ C$.

4 Turbulence in 2 counter-streaming fluids of light

4.1 Dispersion relation

We now consider the case of 2 fluids of light. This part is based on the theoretical work in [1]. One fluid is considered to be at rest while the other is flowing at a velocity \mathbf{v}_0 . As a reminder, the NLSE (5) can be mapped onto the hydrodynamic formulation (7).

The hydrodynamic quantities can be expanded as $\rho_{1,2} = \rho_0/2 + \delta\rho_{1,2}$, $\mathbf{v}_1 = \delta\mathbf{v}_1$, $\mathbf{v}_2 = \mathbf{v}_0 + \delta\mathbf{v}_2$. This is equivalent to NLSE for the superposition $\psi = \psi_1 + \psi_2$. The linear dynamics are evaluated by Fourier decomposition, $\delta\rho_{1,2}(\mathbf{r}_\perp, z) = A_{1,2}e^{i\mathbf{k}\cdot\mathbf{r}_\perp - i\Omega z}$, A_i is the amplitude, \mathbf{k} is the transverse wave vector and Ω the frequency of the elementary excitations, related by the dispersion relation:

$$1 - \frac{1}{2}c_s^2k^2 \left(\frac{1}{\Omega^2 - k^4/4} + \frac{1}{(\Omega - \mathbf{v}_0\cdot\mathbf{k})^2 - k^4/4} \right) = 0, \quad (10)$$

with $c_s = c\sqrt{\Delta n}$ is the fluids speed of sound. In the case of one fluid of light with a density ρ_0 , Ω^2 is equivalent to the Bogoliubov dispersion relation of a weakly interacting Bose gas, describing an acoustic (fluid) regime at low momenta. Remark, the Bogoliubov dispersion relation has been recently measured for a quantum fluid of light in our team [22], [23] (cite fontaine 2018).

We now define the healing length ξ as the scale at which the fluid behavior breaks and turns into a single-particle (massive photon) regime. It is defined as $\xi = \frac{1}{k_0\sqrt{|\Delta n|}}$.

Then the solution of (10) gives:

$$\Omega\xi^2 = \frac{1}{2}k\xi \left(\beta \pm \sqrt{2 + \beta^2 + (k\xi^2 \pm 2\sqrt{1 + 2\beta^2 + \beta^2(k\xi)^2})} \right), \quad (11)$$

where we defined the Mach number $\beta = v_0/c_s$.

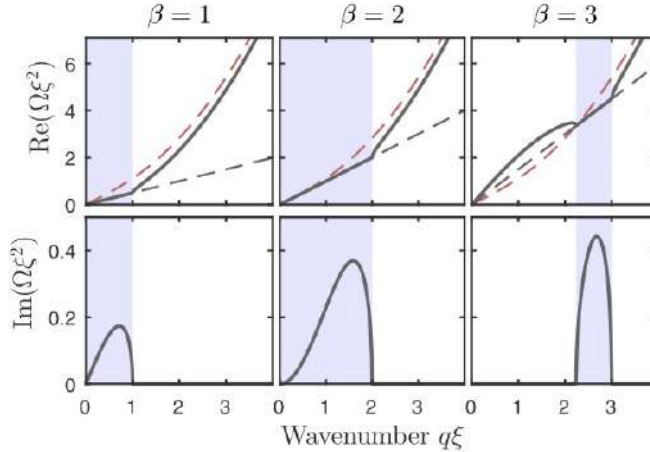


Figure 11: Real and imaginary part of the solutions of the dispersion relation (11) for different fluid velocity. This figure is adapted from [1].

For the conditions $\sqrt{\beta^2 - 4} \leq k\xi \leq \beta$ the imaginary part of the dispersion relation is positive Fig.11. It means that there is an unstable region (as seen in Fig.12) where there is a gain of energy. The system will have to dissipate it by vortex pair generation which will induce instabilities similar to classical hydrodynamics. Experimentally it is in this region that we want to be.

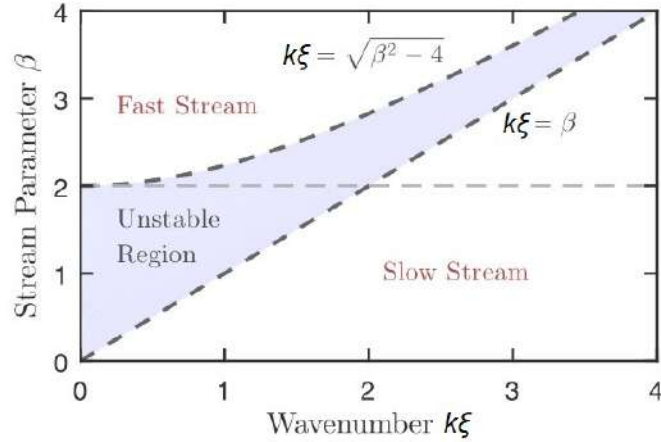


Figure 12: Diagram of the Mach number β as function of the dimensionless value $k\xi$. The 2 dashed lines represent the conditions where the imaginary part is positive. This figure is from [1].

4.2 Experimental setup

Experimentally we use a Spatial Light Modulator (SLM) to separate the beam (1) in 2 counter-streaming beams, (1.1) and (1.2), that we send in the non-linear medium (Rb cell). The scheme is shown in Fig.13.

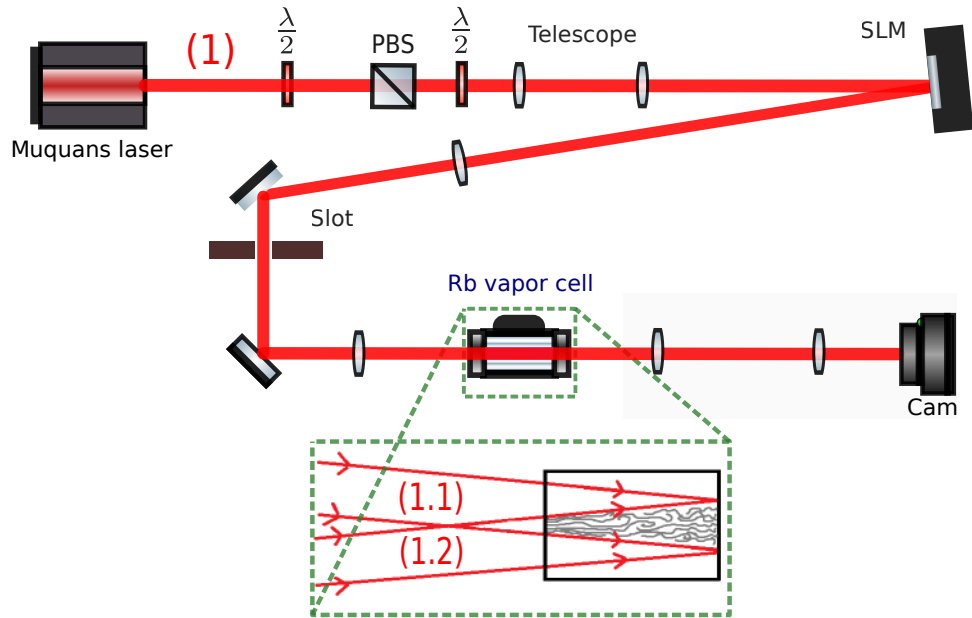


Figure 13: Experimental setup. The PBS allow us to control the power on the setup by changing to polarisation with the first wave plate. A first telescope is used to make the size of the beam larger on the SLM. Then a second one, doing the image of the SLM on the input of the Rb cell. The last telescope is imaging the output of the Rb cell on the camera.

We have control on the transverse wave vector k_{\perp} of beams (1.1) and (1.2) thanks to the SLM (I

will explain in 4.2.1. how this device works).

In the cell the 2 beams are propagating and overlapping along the optical axis as shown on Fig.13. By using large power ($300 \text{ mW} \leq P \leq 1 \text{ W}$) and being close to the resonance ($\Delta \simeq -2 \text{ GHz}$) the non-linearity will be stronger and the field of each beams can be described as the NLSE (5). This is called the non-linear regime in contrast to the linear regime where the non-linearity is zero at small power and far from the resonance ($\Delta \simeq -5 \text{ GHz}$). The reason why the detuning affects the non-linearity is that for large value, the beam will not interact with Rb atoms, and by changing its value we change this interaction.

4.2.1 SLM and fluids velocity control

As a reminder we defined the velocity field as $\mathbf{v} = (c\nabla_{\perp}\phi)/k_0$. It means that changing the phase gives us control on the velocity of the fluids. To do that we use a Spatial Light Modulator (SLM) on which we can print a phase pattern to shape the wavefront of our beam (Fig.14(a)).

The SLM is a device with a small screen that we plug to a computer which recognize it as a second screen. This screen is pixel compound containing liquid crystals. We can control individually each of these pixels by applying a tension to them which will change their birefringence and induce a phase shift. To control it we print on the screen the image we want composed of a 256 levels of grey gradient, white is zero phase shift and black is a 2π phase shift.

For the experiment we use the SLM as a biprism, by printing the Fig.14(b) on the SLM screen, to separate the initial beam (1) in 2 counter-streaming beams (1.1) and (1.2). In addition we print a phase grating which separates the part of the beam that is phase shifted from the rest. The 2 beams are recovered in reflection of the SLM.

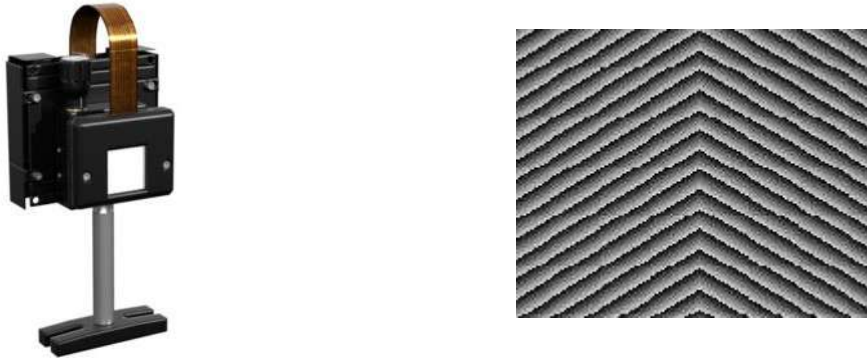


Figure 14: (a) SLM. (b) Phase pattern printed on the SLM working as a biprism

Finally we can control the Mach number β of one beam with the SLM:

$$\beta = \frac{v}{c_s} = \frac{k_{\perp}}{k_0\sqrt{\Delta n}}, \quad (12)$$

Experimentally this amounts to having 2 beams propagating at opposite velocities.

4.2.2 Imaging of interferences evolution in the non-linear medium

We want to observe the evolution of the interference fringes for different propagation times. Experimentally we image only the output of the cell with a camera. Then the linear regime is taken with a large detuning or low power as on Fig.15(a). The non-linear regime is taken for small detuning (near to the resonance) and large power Fig.15(b).



Figure 15: Evolution of the interference fringe : (a) linear case $P = 20$ mW, $\Delta = -5$ GHz and transmission is 100%, (b) non-linear case $P = 300$ mW, $\Delta = -2$ GHz and transmission is 5%. For these data $T = 105^\circ C$ and $k_\perp = 10$ mm $^{-1}$.

After propagating we can see instabilities in the interference fringes shown on Fig.15(b) as predicted by the theory developed in [1].

4.3 Density distribution in the momentum space

To study the turbulence we investigate how the density distribution in the momentum space evolve for linear and non-linear regime.

We image the output of the Rb cell on a camera. In the linear case (i.e large detuning Δ and low power) it is expected that to have fringes (Fig.15(a)) because the 2 counter-streaming beams are interfering together. Then we do the Fourier transform (FT) of the images taken by the camera (Fig.16(a)) and plot the density profile as function of $k_x > 0$ for $k_y = 0$ (Fig.16(b)). In practice, the density profile are plotted by taking the average of the densities on 10 horizontal lines in the center. Similarly, we take 50 pictures while making the beams (1) moving randomly, for exemple by tilting a mirror. Because the instabilities results are random, we normalise this effect to avoid biased measurements. And we want to remove errors due to imperfections present on our lenses, mirrors and on the border of our rubidium cell. The final spectrum is the mean of the 50 FTs.

The distance between the two peaks from the center peak in the Fourier space shown Fig.16(a) gives the value of the wave vector of beams (1.1) and (1.2).

The value of β given on the density profile is calculated from (12). The value of t is equivalent to the propagation time at the input of the medium. The effective $t = 0 \xi / c_s$ is equivalent to saying that the propagation is in the linear regime.

In a second part, we study the evolution of the density profile in the non-linear regime, at $t = 40 \xi / c_s$ for different value of β on Fig.17.

We observe that, for the non-linear regime, the peak width (at $k\xi = \beta$) is larger due to the velocity redistribution. These results are close to what is expected in the theory [1] or [2]. But there are some difference between the theory and the experiment that we need to highlight:

(i) for the turbulent regime the peak (at $k\xi = \beta$) is shifted to smaller value of k this does not appear in the theory. This might be from the defocusing effect caused by the non-linearity which makes the distance between the fringes greater and not the same everywhere. To minimize this effect we can use a flathead (non-Gaussian) beam which allows us to have the same intensity everywhere, which no longer causes this inequality. However, this is difficult to achieve experimentally, instead we use an elongated beam (light sheet) to make the intensity of the beam flatter on the center. Another reason

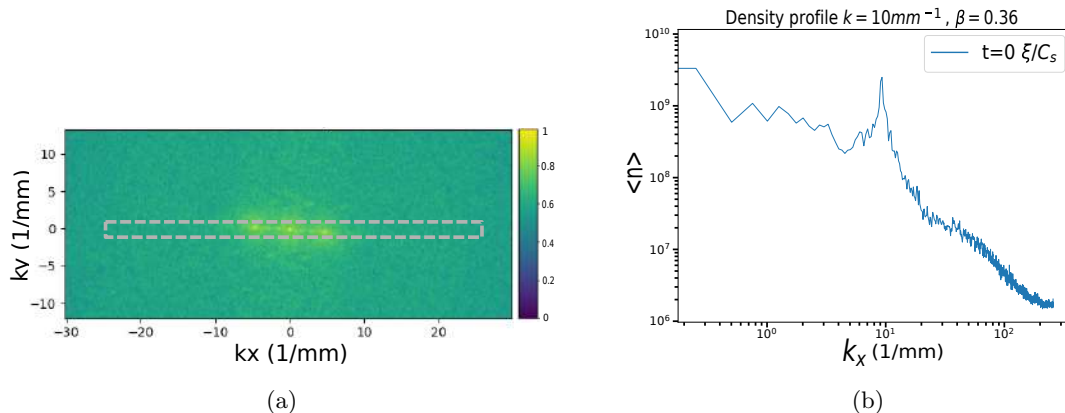


Figure 16: (a) Final FT (average on 50 FTs) of Fig.15(a), the grey dashed region is where the density $\langle n \rangle$ profile is averaged. (b) density profile on 1D line ($k_x > 0$ and $k_y = 0$). For these data $\Delta = -5$ GHz and transmission is 100%, $T = 105^\circ\text{C}$, $k_\perp = 10 \text{ mm}^{-1}$, $P = 50 \text{ mW}$.

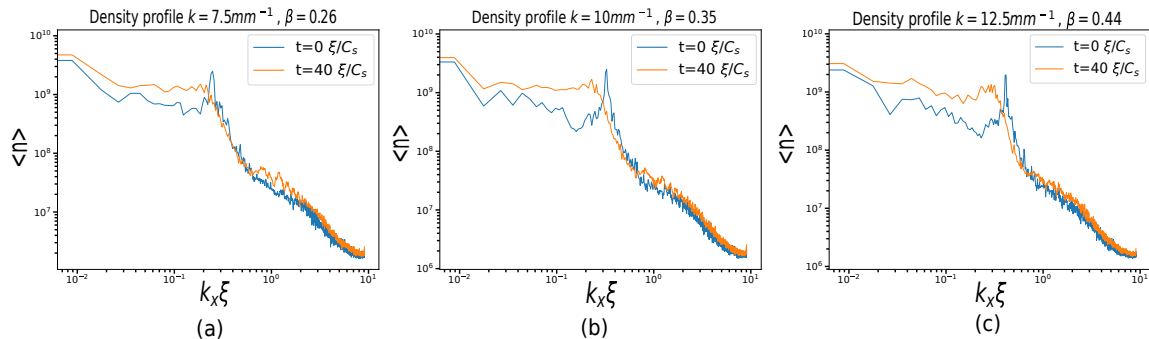


Figure 17: Density profile : (a) $\beta = 0.26$, (b) $\beta = 0.35$, (c) $\beta = 0.44$. The blue and orange curves are respectively the linear and non-linear case. For these data $\Delta = -5$ GHz (transmission is 100%) and $P = 50 \text{ mW}$ for $t = 0 \xi/c_s$. $\Delta = -2$ GHz (transmission is 5%) and $P = 600 \text{ mW}$ for $t = 40 \xi/c_s$, $T = 105^\circ\text{C}$, k_\perp is 7.5, 10 and 12.5 mm^{-1} .

could be because the value of the non-linear refractive index is not constant and changes along the propagation. Moreover, in the theoretical simulations, parameters like the absorption that affects the experiment have not been taken into account.

(ii) the maximum value of β reachable in the experiment is not large enough to explore other regime like the supersonic regime when β is larger than one. In the supersonic regime the light is no longer superfluid because the Landau criterion [24] is outdated. To increase β there are two possibilities. First, make the value of Δn smaller, for example by decreasing the temperature of the medium. The atomic density of the medium will change, and if it is too small, we will not be in the fluids of light regime because the propagation time will be too small. The idea is to find the good balance for the temperature. Secondly, make the value of the velocity fluids larger by applying a higher value of k_\perp on the SLM. But if the wave vector is too large the two beams will not overlap at the output of the medium. To solve this problem we need to use a shorter cell, but if the cell is too short the propagating time will be too small and the instabilities will not have the time to develop enough to become turbulence. Here again it's a matter of balance.

We are working on the improvement of these points. After that, an idea could be to reconstruct the experimental dispersion relation with its imaginary part to know for which value of k_{\perp} the system has a maximum energy gain. Then, we could probe the turbulence with a third beam, which would be at very low power compared to the 2 counter-streaming beams. We will observe a power gain on this one for the values of k where the gain of energy in system the is maximum.

5 Turbulent cascade and vortices

Turbulence is a phenomenon that occurs when the kinetic energy of a flowing fluid becomes too large in relation to the viscosity forces. In the case of superfluids the viscosity is zero. The turbulence comes from the energy gain due to the imaginary part of the dispersion relation. This excess energy will then be dissipated by the system via the generation of vortex pairs. Turbulent cascade is a form of energy transfer between high kinetic energy vortices and smaller ones that absorb and dissipate it. This mechanism is at the origin of the turbulent flow like shown on Fig.18.



Figure 18: Exemple of generation of vortex in a fluid. Source : Etienne Behar

5.1 Optical vortices

Optical vortices are propagating electric field in rotation, for exemple like Laguerre-Gauss beams [25]. The electric field is given by:

$$E(r, \theta, z) = A(r, z) \times e^{i \frac{kr^2}{2R(z)}} \times e^{-i\phi_G(z)} \times e^{-i(kz-\omega t)} \times e^{il\theta}, \quad (13)$$

whith $A(r, z)$ the amplitude field, $R(z)$ the radius of curvature and $\phi_G(z)$ the Gouy phase. Some exemples of intensity images in the transverse plane to the propagation axis are shown Fig.19. This expression is the same as for a Gaussian beam but it contains, in addition, the azimuthal phase term $e^{il\theta}$ which characterises the vortices. This new phase term is also called the Orbital Angular Momentum (OAM). The order of the vortex is given by l .

Thus, a vortex transports the OAM, an additional information dissociated from the polarization and the wave vector.

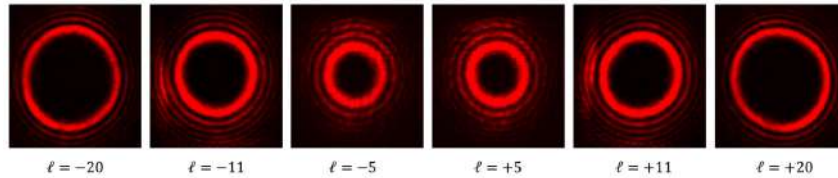


Figure 19: Exemple of vortex images from [26]. These are taken in intensity.

5.2 Phase map and "forks"

The characteristic of a vortex is its wave front having the shape of an ellipsoid as shown on Fig.20. In other words, it means that the phase is doing a $2\pi l$ loop for a vortex of order l . Experimentally this is what we expect to see if, indeed, we have vortices in the system.

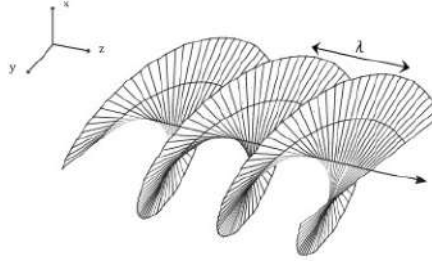


Figure 20: Wavefront of a propagating vortex, here $l = 2$. Figure extracted from [26]

To observe it, we need to reconstruct the phase map of the instabilities. By imaging the output of the cell, we do an interferometer with a reference beam (Fig.21(a)). At some point, we can see dislocation of the fringes, or also called "forks". For example two interference branches will regroup into one. Then, we plot the phase map of the dashed area Fig.21(b). Here we observe phases dislocations ("forks"), for example those who have been surrounded, which means that at those points the phase is doing a 2π loop. In other words, at those points we have a one order vortex.

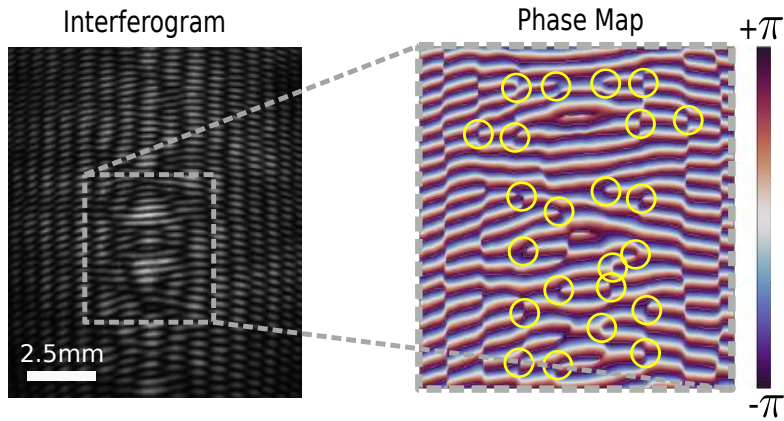


Figure 21: Observation of vortices by reconstructing the phase map using an interferometer. For these data $\Delta = -2$ GHz and transmission is 5%, $T = 105^\circ C$, $k_\perp = 17.5 \text{ mm}^{-1}$, $P = 600$ mW.

These results look alike what other experimental teams saw with their systems, like [27], where they managed to generate 4 vortices in their system. But here the difference is that we have a much larger number of generated vortices randomly distributed.

Another observation is that on both sides of the phase map we see a vertical line where the phase is jumping. This is called solitons [28] which are solitary wave which propagates without being deformed in a nonlinear and dispersive fluids.

5.3 From instabilities to turbulence

To observe how the vortices were generated in the process we plott the images of the instabilities for different values of the power with the phase map associated (Fig.22). By increasing the power we increase the non-linearity and the regime is more and more turbulent. The linear case has been taken for $P=20$ mW and far from the resonance.

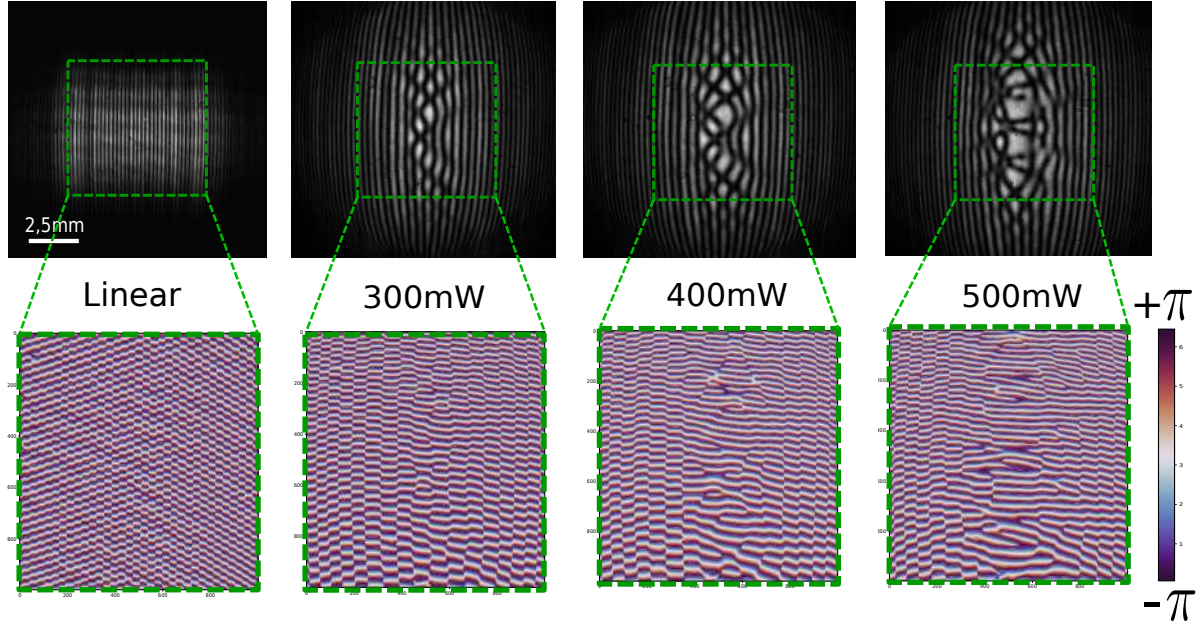


Figure 22: Evolution of the instabilities and the phase associated for different value of the power. All of the phase map are reconstructed from the green dashed region. The colormap indicates that the phase makes one round of $-\pi$ to $+\pi$. For these data $\Delta = -2$ GHz and transmission is 5%, $T = 105^\circ C$, $k_\perp = 17.5 \text{ mm}^{-1}$.

Linear regime : we observe on the sides the same phase pattern printed on the SLM.
 $P=300$ mW : there are instabilities in the interference fringes, also called "snakes" instabilities [29]. These are due to the propagation of contra-propagating solitons that eventually break up [30]. A few vortices are generated at the center as we can see on the phase map.
 $P=400$ mW : the instabilities begins to break faster and harder, as we can see, we have more vortices generated and the system begins to be more chaotic.
 $P=500$ mW : Here the system is in the turbulent regime. At this point we have much more generated vortices randomly distributed.

6 Conclusion

Building on the theoretical work of other group on quantum fluids of light ([1], [2]), we have succeeded in making the first experimental realisation and observation of quantum turbulence for fluids of light in hot atomic vapours.

Light propagating in the paraxial approximations can be described as a quantum fluids [8] and then the phenomenon of turbulence can be observed. In this work I described the experimental realisation of turbulence with 2 counter-streaming fluids of light.

This has been achieved by separating and controlling the velocity of each fluids and imposing opposite speeds on them. We then study the evolution of the interference fringes for different propagation times. We observe the appearance of increasingly pronounced "snake" instabilities until we reach the turbulent regime where their shape becomes completely random.

Then, by studying the density distribution in the momentum space and by varying the configurations and propagation times of our fluids, we have observed the effect of the velocity redistribution. Moreover we identified the differences between the theoretical simulations and our experimental results, and discussed applications to reduce these differences.

Finally, we have reconstructed the phase map of our beams in order to highlight the presence of pairs of generated elementary vortices. Their presence is a response of the system to dissipate the energy gain explained by the positive imaginary part of the dispersion relation.

This work open the way to the study of transitions in out-of-equilibrium dynamics in superfluids of light. In the next stage of our work, we would like to develop the necessary tools to be able to perform the first experimental proof of the turbulent cascade in quantum fluids of light.

References

- [1] João D Rodrigues, José T Mendonça, and Hugo Terças. Turbulence excitation in counterstreaming paraxial superfluids of light. *Physical Review A*, 101(4):043810, 2020.
- [2] Nuno Azevedo Silva, Tiago D Ferreira, and Ariel Guerreiro. Exploring quantum-like turbulence with a two-component paraxial fluid of light. *Results in Optics*, 2:100025, 2021.
- [3] Quentin Fontaine. Paraxial fluid of light in hot atomic vapors. November 2020. *Physical Review A*.
- [4] André Kolmogorov. Théorie générale des systèmes dynamiques de la mécanique classique. *Séminaire Janet. Mécanique analytique et mécanique céleste*, 1:1–20, 1957.
- [5] Patrick Chassaing. *Mécanique des fluides*. 2000.
- [6] Lev Pitaevskii and Sandro Stringari. Uncertainty principle, quantum fluctuations, and broken symmetries. *Journal of low temperature physics*, 85(5):377–388, 1991.
- [7] Victor Nikolaevich Popov. Hydrodynamic hamiltonian for a nonideal bose gas. *Theoretical and Mathematical Physics*, 11(2):478–486, 1972.
- [8] Iacopo Carusotto and Cristiano Ciuti. Quantum fluids of light. *Reviews of Modern Physics*, 85(1):299, 2013.
- [9] Murad Abuzarli, Tom Bienaimé, Elisabeth Giacobino, Alberto Bramati, and Quentin Glorieux. Blast waves in a paraxial fluid of light. *EPL (Europhysics Letters)*, 134(2):24001, 2021.
- [10] Anne Maitre, Giovanni Lerario, Adrià Medeiros, Ferdinand Claude, Quentin Glorieux, Elisabeth Giacobino, Simon Pigeon, and Alberto Bramati. Dark-soliton molecules in an exciton-polariton superfluid. *Physical Review X*, 10(4):041028, 2020.

- [11] Robert W Boyd. *Nonlinear optics*. Academic press, 2020.
- [12] E Cumberbatch. Self-focusing in non-linear optics. *IMA Journal of Applied Mathematics*, 6(3):250–262, 1970.
- [13] Quentin Fontaine, Pierre-Élie Larré, Giovanni Lerario, Tom Bienaimé, Simon Pigeon, Daniele Faccio, Iacopo Carusotto, Élisabeth Giacobino, Alberto Bramati, and Quentin Glorieux. Interferences between bogoliubov excitations in superfluids of light. *Physical Review Research*, 2(4):043297, 2020.
- [14] Erwin Madelung. Quantentheorie in hydrodynamischer form. *Zeitschrift für Physik*, 40(3):322–326, 1927.
- [15] Quentin Glorieux. Quantum optics in dense atomic media: From optical memories to fluids of light. *arXiv preprint arXiv:1812.08602*, 2018.
- [16] Paul Siddons, Charles S Adams, Chang Ge, and Ifan G Hughes. Absolute absorption on rubidium d lines: comparison between theory and experiment. *Journal of Physics B: Atomic, Molecular and Optical Physics*, 41(15):155004, 2008.
- [17] Lee Weller, Robert J Bettles, Paul Siddons, Charles S Adams, and Ifan G Hughes. Absolute absorption on the rubidium d1 line including resonant dipole–dipole interactions. *Journal of Physics B: Atomic, Molecular and Optical Physics*, 44(19):195006, 2011.
- [18] Omar Boughdad, Aurélien Eloy, Fabrice Mortessagne, Matthieu Bellec, and Claire Michel. Anisotropic nonlinear refractive index measurement of a photorefractive crystal via spatial self-phase modulation. *Optics express*, 27(21):30360–30370, 2019.
- [19] GA Swartzlander, H Yin, and AE Kaplan. Continuous-wave self-deflection effect in sodium vapor. *JOSA B*, 6(7):1317–1325, 1989.
- [20] Neven Šantić, Adrien Fusaro, Sabeur Salem, Josselin Garnier, Antonio Picozzi, and Robin Kaiser. Nonequilibrium precondensation of classical waves in two dimensions propagating through atomic vapors. *Physical review letters*, 120(5):055301, 2018.
- [21] CF McCormick, DR Solli, RY Chiao, and JM Hickmann. Saturable nonlinear refraction in hot atomic vapor. *Physical Review A*, 69(2):023804, 2004.
- [22] Q Fontaine, T Bienaimé, S Pigeon, E Giacobino, A Bramati, and Q Glorieux. Observation of the bogoliubov dispersion in a fluid of light. *Physical review letters*, 121(18):183604, 2018.
- [23] Clara Piekarski, Wei Liu, Jeff Steinhauer, Elisabeth Giacobino, Alberto Bramati, and Quentin Glorieux. Short bragg pulse spectroscopy for a paraxial fluids of light. *Physical Review Letter*, 127,023401, 2020.
- [24] Seth J Putterman. Superfluid hydrodynamics. *Amsterdam*, 3, 1974.
- [25] Victor V Kotlyar, Svetlana N Khonina, Anton A Almazov, Victor A Soifer, Konstantins Jefimovs, and Jari Turunen. Elliptic laguerre-gaussian beams. *JOSA A*, 23(1):43–56, 2006.
- [26] Aurelien Chopinaud. Atomes et vortex optiques : conversion de moments orbitaux de lumière en utilisant la transition à deux photons 5s-5d du rubidium. *tel-01941723*, June 2018.
- [27] Aurélien Eloy, Omar Boughdad, Mathias Albert, Pierre-élie Larré, Fabrice Mortessagne, Matthieu Bellec, and Claire Michel. Experimental observation of turbulent coherent structures in a superfluid of light. *arXiv:2012.13280*, 2020.

- [28] Jacek Dziarmaga. Quantum dark soliton: Nonperturbative diffusion of phase and position. *Physical Review A*, 70(6):063616, 2004.
- [29] Ferdinand Claude, Sergei V Koniakhin, Anne Maître, Simon Pigeon, Giovanni Lerario, Daniil D Stupin, Quentin Glorieux, Elisabeth Jacobino, Dmitry Solnyshkov, Guillaume Malpuech, et al. Taming the snake instabilities in a polariton superfluid. *Optica*, 7(12):1660–1665, 2020.
- [30] Anne Maitre, Ferdinand Claude, Giovanni Lerario, Serguei Koniakhin, Simon Pigeon, Dmitry Solnyshkov, Guillaume Malpuech, Quentin Glorieux, Elisabeth Jacobino, and Alberto Bramati. Spontaneous generation, enhanced propagation and optical imprinting of quantized vortices and dark solitons in a polariton superfluid: towards the control of quantum turbulence. *arXiv:2102.01075*, 2021.